Volatile Resistive Switching Memory Based on Ag Ion Drift/Diffusion—Part II: Compact Modeling

Wei Wang, *Member, IEEE*, Mario Laudato, Elia Ambrosi, Alessandro Bricalli, Erika Covi, *Member, IEEE*, Yu-Hsuan Lin, and Daniele Ielmini, *Fellow, IEEE*

***Abstract*—Resistive-switching random access memory (RRAM) based on Cu or Ag filament is a promising selector device for high-density crosspoint arrays. These devices display high ON-OFF ratio, volatile switching, high switching speed, and long endurance, supporting the adoption in large memory arrays. However, the mechanism of volatile switching is not clear yet, which prevents the development of compact models for circuit design and simulation. Based on an extensive study of the switching mechanism, we report an analytical model that captures all electrical characteristics of the device, including switching, recovery, and their dependence on the applied voltage. We use the analytical model to simulate the circuit-level behavior of the device as long/short term memory synapse.**

***Index Terms*—Analytical model, neuromorphic computing, retention time, selective device, volatile switching.**

I. Introduction

VOLATILE resistive-switching random access memory (RRAM) based on Ag and Cu migration is a new type of device featuring high ON-OFF resistance ratio, fast switching, and tunable relaxation time. Recent studies have reported volatile RRAM with excellent properties, such as high ON-OFF resistance ratio approaching 10^{10} [1], [2], steep subthreshold slope less than 1 mV/dec [3], and high endurance up to 10^{10} cycles [4]. The high ON-OFF resistance ratio and unstable ON-state enable applications as selector device for accessing individual elements in large cross-point arrays for high-density data storage [5]–[8], and sensor arrays for high-resolution environment perception [1]. The relaxation time, namely, the lifetime of the ON-state or low resistance state (LRS), can be controlled by the filament size, hence the compliance current I_C [9]. The controllable relaxation time provides further opportunities of application in neuromorphic computation systems, as the device can mimic the short/long term memory effect of biological synapses [10]–[12]. To enable the application of the volatile RRAM in crosspoint arrays and neuromorphic systems, circuit-level design and simulation are essential. To this purpose, a physics-based model with low computational cost and capability to accurately predict the current–voltage (I–V) characteristics of the device is highly demanded.

In this paper, we carry out an experimental and simulation analysis of the metallic filament disruption process in the volatile device. By a physical study of the metallic filament break process of the volatile device, we obtain a filament size spontaneous evolution equation, which will act as the device relaxation model. By combining the filament relaxation model with a previous RRAM model for voltage-controlled filament growth [13], we develop a physics-based analytical model for volatile RRAM. The model accurately captures the device characteristics, such as dc and ac switching curves and retention characteristics. By including the statistical spread of the activation energy, stochastic variations are also described.

A preliminary study of the physics-based modeling of the volatile device was previously reported [14]. Here, we provide an extensive report with full details on the development, validation, and applications of the analytical model. The physical basis of filament size spontaneous evolution is provided, full details of the derivation of all equations are given, and the application of the volatile devices with tunable retention time for spatiotemporal spiking neural network is demonstrated. The model with simple equations and physical basis can be readily implemented in a Verilog-A type SPICE model for circuit simulations.

II. Filament Relaxation Model

Fig. 1 shows a schematic illustration of the I–V curves for a nonvolatile RRAM (a) and a volatile RRAM (b). In the latter

Manuscript received May 18, 2019; revised July 3, 2019; accepted July 10, 2019. Date of publication August 5, 2019; date of current version August 21, 2019. This work has received funding from the European Research Council (ERC) under the European Union's Horizon 2020 Research and Innovation Programme (Grant Agreement No. 648635) and from Ministero dell'Istruzione dell'Università e della Ricerca (Grant Agreement No. 2016/R164TYLBZP). This work was partially performed at Polifab, the micro- and nanofabrication facility of Politecnico di Milano. The review of this paper was arranged by Editor P. Du. *(Corresponding author: Daniele Ielmini.)*

W. Wang, M. Laudato, E. Ambrosi, A. Bricalli, E. Covi, and D. Ielmini are with the Dipartimento di Elettronica, Informazione e Bioingegneria, Politecnico di Milano, 20133 Milan, Italy (e-mail: daniele.ielmini@polimi.it).

Y.-H. Lin is with the Department of Electronics Engineering, Institute of Electronics, National Chiao Tung University, Hsinchu 30010, Taiwan, and also with the Dipartimento di Elettronica, Informazione e Bioingegneria, Politecnico di Milano, 20133 Milan, Italy.

Color versions of one or more of the figures in this article are available online at http://ieeexplore.ieee.org.

Digital Object Identifier 10.1109/TED.2019.2928888

This work is licensed under a Creative Commons Attribution 4.0 License. For more information, see http://creativecommons.org/licenses/by/4.0/

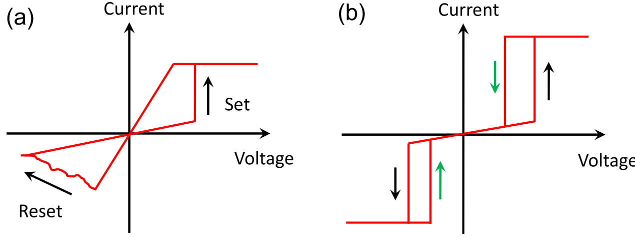

Fig. 1. Typical I–V curves of (a) nonvolatile and (b) volatile RRAM devices.

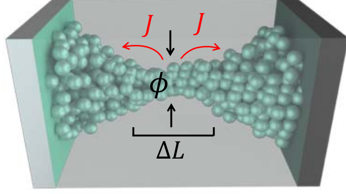

Fig. 2. Schematic of the filament atoms migration toward two electrodes and the narrowing of filament diameter in the bottleneck region.

type of device, the conductive filament (CF) formed at the set process is not stable, thus the device cannot maintain its LRS or ON-state. As a result, the transition to the ON-state for the volatile RRAM is similar to the set transition of the nonvolatile RRAM, while the spontaneous "reset" transition is missing in the previous nonvolatile RRAM models [15]–[18]. As pointed out in previous studies [9], [14], the CF relaxation process consists of two phases, namely CF diameter narrowing, which leads to the CF disconnection, and CF retraction, where the remaining fragments of the CF reduce their extension toward the top and bottom electrodes.

A. CF Disconnection Process

Fig. 2 schematically shows the CF narrowing process in the volatile RRAM, where the filament atoms spontaneously migrate from the central region of the filament to the two electrodes, driven by the tendency of surface energy minimization [13]. The energy minimization drives the migration of atoms from regions with high curvature to others with lower curvature, which results in a reduction of the CF diameter ϕ [9].

The current density of atomic diffusion can be written as [9], [19]

$$J \approx \left(\frac{D_s \gamma \delta}{k_B T}\right) \frac{\kappa - \kappa'}{\Delta L/2} \approx \left(\frac{D_s \gamma \delta}{k_B T}\right) \phi^{-2} \tag{1}$$

where D_s is the surface diffusion coefficient, γ is the surface tension, δ is the interatomic distance, k_B is the Boltzmann's constant, T is the temperature, and κ is the CF surface curvature at a bottleneck point, supposed to be located around the middle of the CF. In (1), this curvature is compared to κ' at an adjacent point with an offset of $\Delta L/2$, where ΔL is an effective length of the bottleneck region with an infinitesimal value. The two curvatures can thus be approximated as $1/\phi$ and $1/(\phi + \Delta L/2)$, respectively. The thermally activated surface diffusion coefficient is given by [20]

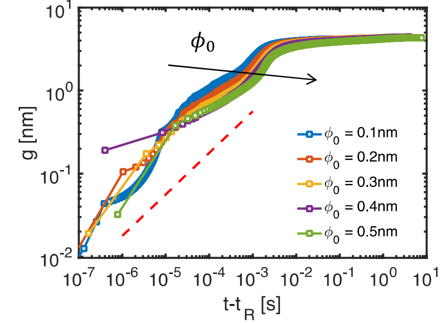

Fig. 3. CF gap g as a function of time t–t_R from the filament break event.

$$D_s = D_s' e^{-\frac{E_{\text{surf}}}{k_B T}} \tag{2}$$

where D_s' is a preexponential factor and E_{surf} is the energy barrier for surface diffusion. The volume decrease rate with time at the CF bottleneck region can thus be estimated as

$$\frac{dU}{dt} = -2J \cdot \Delta L \cdot \delta^3. \tag{3}$$

From the relationship between volume change and CF diameter change, which is given by

$$\frac{dU}{dt} = \frac{d\phi}{dt} \pi \phi \frac{\Delta L}{2} \tag{4}$$

we can derive the narrowing rate

$$\frac{d\phi}{dt} = -\frac{4 D_s' \gamma \delta^4}{\pi k_B T} \phi^{-3} e^{-\frac{E_{\text{surf}}}{k_B T}} \tag{5}$$

where (1)–(4) have also been used. From (5), we obtain

$$t_R = \int dt \propto -\int_{\phi_0}^{0} \phi^3 d\phi \tag{6}$$

where ϕ_0 is the diameter of the initial CF. Integration of (6) yields

$$t_R \sim \phi_0^4, \tag{7}$$

which is consistent with the size-dependent relaxation time obtained from in previous studies [9], [13], [14].

The CF narrowing process in (5), which describes the volatile behavior of the RRAM device, is a self-accelerated process. In fact, a decrease of the CF diameter ϕ further increases the narrowing rate $(d\phi)/(dt)$, which supports a fast transition to the OFF-state. The limit $\phi \to 0$ has no physical meaning in (5) since the filament continuity does no longer exist when its diameter is smaller than the atomic diameter ϕ_a.

B. CF Retraction Process

After the relaxation time, i.e., the time t_R for which the CF diameter reaches $\phi = 0$, the remaining CF fragments retract to the electrodes, in agreement with molecular dynamics (MD) and numerical simulation results [13]. Fig. 3 shows the calculated gap length g across the CF as a function of time after disconnection,

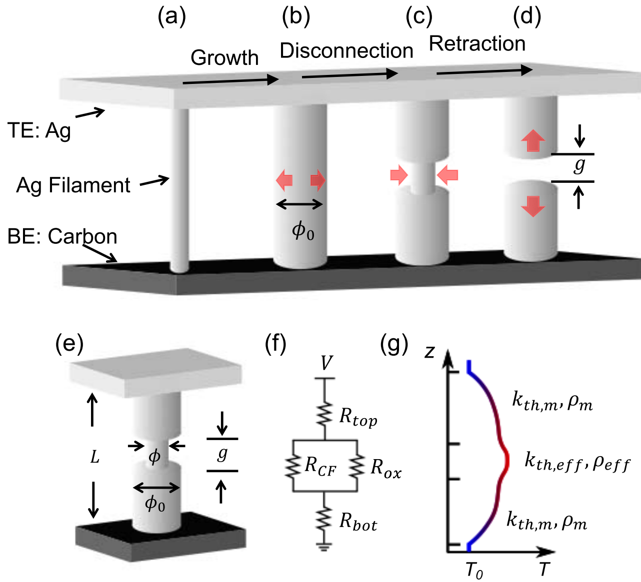

Fig. 4. Schematic of the analytical modeling of volatile RRAM device. (a)–(d) Filament shape evolution during switching. (a) and (b) Filament growth under the electrical field. (b) and (c) Filament disconnection induced by diameter narrowing in its bottleneck. (c) and (d) Stub retraction after filament break. (e) Parameters used for conductance and filament temperature. (f) Series resistor model for device conductance calculation. (g) Parameters for and illustration of the temperature profile.

according to our numerical surface diffusion model [13] (data in Fig. 3 and from simulation results shown in Fig. 7 of the companion paper [13]) for the initial diameter ϕ_0 changing from 0.1 to 0.5 nm. Observing power-law dependence of the g on time, simulation results for various initial diameter ϕ_0 can be approximately described by an empirical equation

$$g = g_0(t - t_R)^\beta t > t_R \tag{8}$$

where g_0 and β are fitting parameters controlling the retraction speed. Changing filament initial diameter only slightly alters the time course of the CF fragment retraction. This can be understood as that the filament retraction is dominated by the surface diffusion in the vertical direction, which is only slightly affected by the CF diameter.

III. Analytical Model

A. Narrowing and Retraction Models

Fig. 4 shows a schematic illustration of the analytical model for drift and diffusion for an Ag-based volatile RRAM device [14]. First, the CF is formed at a set transition, consisting of CF growth as a result of field-induced drift of Ag from the positively biased electrode [Fig. 4(a) and (b)]. The set transition can be described by a field-driven, temperature-activated migration model, similar to conventional nonvolatile RRAMs [21]. By combining the CF growth [Fig. 4(a) and (b)] and disconnection processes [Fig. 4(c)], we thus obtain

$$\frac{d\phi}{dt} = \left.\frac{d\phi}{dt}\right\|_{\text{drift}} + \left.\frac{d\phi}{dt}\right\|_{\text{diff}} = Ae^{-\frac{E_{\text{bulk}}-\alpha qV}{k_B T}} - C\phi^{-3}e^{-\frac{E_{\text{surf}}}{k_B T}} \quad \phi \geq \phi_a \tag{9}$$

where A and C are preexponential factors, E_{bulk} is the energy barrier for field-driven drift, q is the elementary charge, V is the applied voltage, and α is a barrier lowering coefficient. The first term in the right-hand side of (9) describes CF growth while the second term accounts for the narrowing process of (6) with $C = (2D_s{}'\gamma\delta^4)/(\pi k_B T)$. The condition $\phi \geq \phi_a$ ensures that $(d\phi)/(dt)\|_{\text{diff}}$ has a finite value for vanishing ϕ. For $\phi < \phi_a$, the diameter is approximated to zero when calculating the device resistance and temperature profile.

The cooperation/competition of drift and diffusion in (9) is responsible for the dynamics of volatile RRAM [22]. For large applied V, drift dominates over diffusion, thus causing the CF growth [Fig. 4(a) and (b)]. On the other hand, for low-bias or unbiased conditions, diffusion dominates thus resulting in the spontaneous CF narrowing process [Fig. 4(c)]. After CF relaxation, retraction can then be calculated by (8).

To further simplify the model, we assumed that the narrowing process only takes place across a minimum region close to the middle of the CF [Fig. 4(c)]. The length of the minimum region is defined as g_a, which is also the initial gap for the stub retraction after the filament break event. The diameter of the rest of the CF is assumed equal to ϕ_0, namely, the maximum diameter achieved during the growth process. This approximation is acceptable since the CF conductance is dominated by the bottleneck diameter and by the gap length in the narrowing and retraction phases, respectively.

B. Conductance and Heating Models

Fig. 4(e) shows the device geometry while Fig. 4(f) shows the corresponding resistance network, from which the device resistance R is given by

$$R = R_{\text{top}} + R_{\text{bot}} + R_{\text{CF}}||R_{\text{ox}} \tag{10}$$

where R_{top} and R_{bot} are the resistances of top and bottom regions of the CF with diameter ϕ_0, R_{CF} is the resistance of the bottleneck region of the CF, and R_{ox} is the resistance of the oxide material surrounding (or replacing) the bottleneck region. The resistance values are given by

$$\begin{cases} R_{\text{top}} + R_{\text{bot}} \approx 4\rho_{\text{m}}\,(L-g)\,/\phi_0^2 \\ R_{\text{CF}} \approx 4\rho_{\text{m}} L/\phi^2 \\ R_{\text{ox}} \approx 4\rho_{\text{ox}} g/\,(\phi_0-\phi)^2\,. \end{cases} \tag{11}$$

In (11), the metal resistivity ρ_{m} is written according to an electron scattering model [23], [24], namely,

$$\rho_{\text{m}} = \rho_{\text{m0}}\frac{1 - p\,l_{\text{f}}}{1 + p\,\phi} \tag{12}$$

where ρ_{m0} is the bulk metal resistivity, p is the fraction of electrons scattered at the surface, and l_{f} is the electron mean free path. The oxide resistivity ρ_{ox} is given by

$$\rho_{\text{ox}} = \frac{\rho_{\text{ox0}}}{1 + \gamma F} \tag{13}$$

where ρ_{ox0} is the bulk oxide resistivity and γ is a constant describing the nonlinear transport due to, e.g., Poole–Frenkel effect [25].

To evaluate T in (9), we used the maximum temperature along the profile calculated by a simplified Joule heating

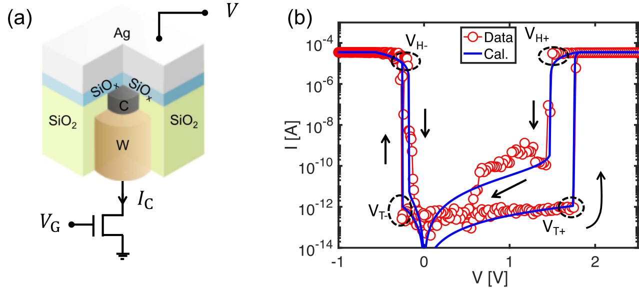

Fig. 5. (a) Schematic of one volatile switching device–one transistor configuration for device characteristics. (b) Comparison between experimental and calculated dc characteristics of the volatile switching device.

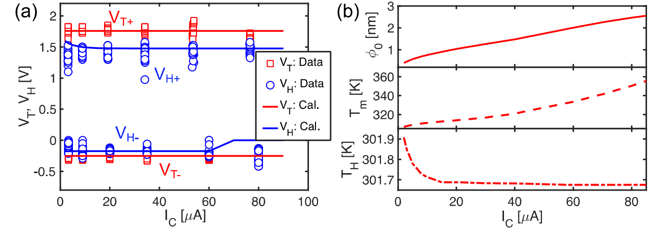

Fig. 6. (a) Threshold voltage and holding voltage under both positive and negative bias extracted from experimental data and calculation results, as a function of compliance current. (b) Calculated maximum filament diameter, maximum temperature (T_m) and temperature at hold voltage (T_H) as a function of compliance current.

TABLE I
MODEL PARAMETER VALUES

Parameter	Positive Bias	Negative Bias
E_{bulk}	Mean: 0.99 eV Std.: 0.015 eV	Mean: 0.65 eV Std.: 0.02 eV
E_{surf}	Mean: 0.65 eV Std.: 0.01 eV	Mean: 0.52 eV Std.: 0.02 eV
α	0.28	1.1
A	$100\ \text{m}\cdot\text{s}^{-1}$	
C	$3\times10^{-26}\ \text{m}^4\cdot\text{s}^{-1}$	
ρ_{m0}	$2\ \mu\Omega\cdot\text{m}$	
p	0.5	
l_f	28 nm	
γ	$5.5\times10^{-8}\ \text{m}\cdot\text{V}^{-1}$	
ρ_{ox0}	$2\times10^4\ \Omega\cdot\text{m}$	
$k_{th,m}$	$5\times10^3\ \text{W}\cdot\text{m}^{-1}\text{K}^{-1}$	
$k_{th,ox}$	$1\ \text{W}\cdot\text{m}^{-1}\text{K}^{-1}$	
g_0	$1\times10^{-9}\ \text{m}\cdot\text{s}^{-0.5}$	
β	0.5	
ϕ_a	0.1 nm	
g_a	0.2 nm	

model. This is obtained by integrating the Fourier equation and calculating the temperature profile along the filament, resulting in the T given by [26]

$$T = T_0 + \frac{J^2\rho_m}{8k_{th,m}}(L^2 - g^2) + \frac{J^2\rho_{eff}}{8k_{th,eff}}g^2 \tag{14}$$

where T_0 is the ambient temperature, J the current density, $k_{th,m}$ is the thermal conductivity of the metal, $\rho_{eff} = \phi_0^2(\rho_m/\phi^2 || \rho_{ox}/(\phi_0^2 - \phi^2))$ is the effective resistivity, and $k_{th,eff} = \phi^2/\phi_0^2 k_{th,m} + (1 - \phi^2/\phi_0^2)k_{th,ox}$ is the effective thermal conductivity of the bottleneck region incorporating the CF and the surrounding oxide with thermal conductivity $k_{th,ox}$. Fig. 4(g) shows a typical temperature profile from (14).

IV. SIMULATION RESULT

A. DC Characteristics

Fig. 5(a) shows the structure of the volatile RRAM with Ag/SiO_x/C stack and a select transistor to control the maximum current, namely I_C [27]. The thickness of the dielectric layer was L = 5nm. Fig. 5(b) shows the dc characteristics measured after forming for $I_C = 35\mu$A [28]. The device shows switching from the OFF-state (about 10^{-12} A) to the ON-state ($I_C = 10^{-5}$ A) in correspondence of the threshold voltage V_{T+}, followed by a recovery of the OFF-state as the voltage is reduced below a characteristic holding voltage V_{H+}, which marks the CF disconnection. Calculations by (9)–(14) with the parameters in Table I are also shown. All these values are in reasonable agreement with the range reported in the literature [21], [26]. The high ON-OFF ratio ($>10^7$) and steep switching slope (<4 mV/dec) are well captured by the model. Note that the current drops to about 0.1 nA in correspondence of V_H, which is higher than the fully-relaxed OFF-state. This can be explained by the relatively-slow stub retraction after CF disconnection. The gradual retraction and the consequent hysteresis are accurately captured by the analytical model, which is missing in the Monte Carlo model in the companion paper (Fig. 2(b) in ref. [13]). The residual current along the voltage sweep back below 1 nA is not frequently reported in similar devices [3], [29], except for [30]. The absence of this residual kick-off current might be due to the very fast retraction of the filament compared to the timescale for applying a dc sweeping voltage. By adjusting the filament retraction parameters, the model can also reproduce I–V curves with fast retraction and no hysteresis in the sub-nA regime. Also note that, due to the asymmetric device structure shown in Fig. 5(a), switching voltages are typically smaller for negative voltage than for positive voltage [27]. To describe this effect, different values of E_{bulk} and α were used in the model as summarized in Table I. These values of the activation energies in Table I can be interpreted as effective activation energies for the best fitting of the I–V characteristics.

Fig. 6(a) shows the measured and calculated switching voltages, namely, V_{T+}, V_{H+}, V_{T-} and V_{H-}, as a function of I_C [27]. The calculation results agree with the experimental data in the broad range from 0.1 to 80 μA. Note that threshold and holding voltages are almost constant across the I_C range. This can be understood by calculating the switching voltages from (9) in correspondence of $d\phi/dt = 0$, which leads to

$$V_T = \frac{k_B T}{q\alpha}\log\left(\frac{C}{A}\frac{1}{\phi_a^3}\right) + \frac{E_{bulk} - E_{surf}}{q\alpha} \tag{15}$$

$$V_H = \frac{k_B T}{q\alpha}\log\left(\frac{C}{A}\frac{1}{\phi_0^3}\right) + \frac{E_{bulk} - E_{surf}}{q\alpha} \approx \frac{E_{bulk} - E_{surf}}{q\alpha}. \tag{16}$$

While V_T in (15) is obviously independent of I_C, V_H in (16) shows a dependence on ϕ_0 and temperature at hold voltage T_H, which changes with I_C as shown by calculations

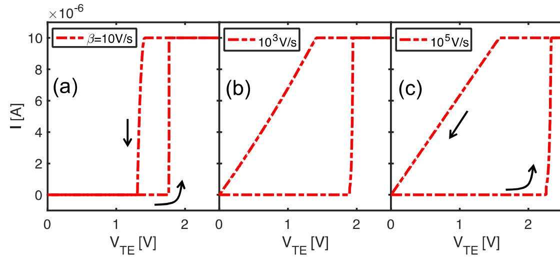

Fig. 7. Quasi-dc *I–V* characteristics for different sweep rates (a) 10 V/s, (b) 10^3 V/s, and (c) 10^5 V/s.

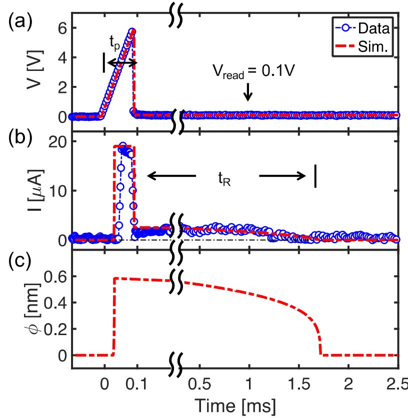

Fig. 8. Measured and simulated ac characteristics of the volatile device. (a) Applied voltage (a half triangular pulse with width $t_p = 100\ \mu$s and following with small read voltage 0.1 V). (b) Measured and simulated current response. (c) Simulated filament diameter evolution.

in Fig. 6(b) [14]. As a result, V_H slightly decreases with increasing I_C, which is due to the higher stability of the relatively thick CF at high I_C. The maximum value of the calculated filament temperature T_m from 300 to 360 K shown in Fig. 6(b) is relatively low compared to oxygen-based filamentary RRAM devices [31], and is consistent with *ab initio* calculations of Ag-based RRAM devices [32]. The relatively low temperature of the Ag filament can be explained by the higher thermal conductivity of the metallic filament.

Fig. 7 shows calculated I–V curves at variable voltage sweep rate, namely, dV/dt = 10 V/s (a), 10^3 V/s (b) and 10^5 V/s (c). As dV/dt increases, V_T increases from 1.7 to 2.2 V, due to the time-voltage relationship of the ionic drift process in (9). The decrease of V_H with increasing dV/dt is instead due to the finite diffusion rate in (5). At sufficiently fast sweep rate, the vanishing time of the applied voltage becomes faster than the relaxation time of the CF, thus preventing the observation of the CF disconnection within the sweep time.

B. AC Characteristics

Fig. 8 shows the (a) voltage and (b) current measured during the application of a half triangular pulse with $t_p = 100\ \mu s$ and peak amplitude 6 V, followed by a constant read voltage $V_{read} = 0.1$ V applied to the device. A compliance current $I_C = 20\ \mu$A was forced via the select transistor. After the steep increase in correspondence of the set transition, the current shows a decay behavior with a retention time t_R of about

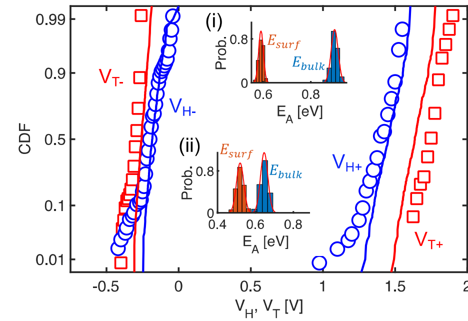

Fig. 9. Distributions of measured (symbols) and calculated (lines) threshold voltage and holding voltage of the volatile RRAM, with insets showing the distributions of activation energies for (i) positive bias and (ii) negative bias.

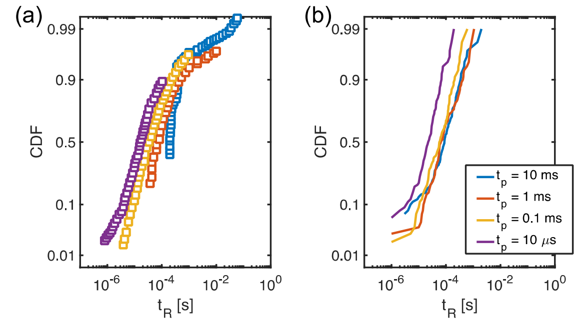

Fig. 10. (a) and (b) Distributions of the measured and calculated retention time t_R for increasing pulsewidth t_p.

1.5 ms. The figure also shows the calculated voltage and current, as well as the CF diameter in Fig. 8(c). As the voltage is switched to the read level, the CF diameter first decreases slowly then steeply drops to zero, in agreement with the self-accelerated process in (5). The decrease of the CF marks the retention time in Fig. 8(b).

C. Statistical Variations

Experimental data of the volatile RRAM device in both dc and ac measurement show a large statistical variability. While variations may hinder the selector applications of the volatile devices, they may also support stochastic device behavior for neuromorphic computing [33], [34] and true random number generation [35], [36]. In either case, accurate modeling of the statistical variability is essential.

Note that the variation of the threshold and hold voltages generally follows Gaussian distribution while the variation of the retention time follows a log-normal distribution, as shown in Figs. 9 and 10, respectively. This can be explained by (9), where the time-related term, i.e., the speed of the filament evolution, is governed by an exponential function of the voltage. As a result, a source of variation with Gaussian distribution of the parameters in the exponent, i.e., the activation energies, can be intuitively expected [37], [38]. To describe the stochastic variations in the volatile RRAM, we assumed a Gaussian distribution of E_{bulk} and E_{surf}, as shown in the insets of Fig. 9. The standard deviations of the Gaussian distribution are given in Table I. Including these variations in Monte

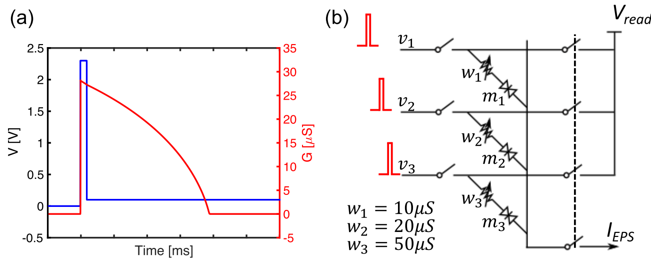

Fig. 11. (a) Short-memory effect represented by the conductance decay of the volatile device. (b) Schematic of the circuit with RRAM synapses to detect spike sequence. Each synapse consists of one nonvolatile RRAM weighting element (w_1, w_2, or w_3) and one volatile RRAM short memory (m_1, m_2, or m_3).

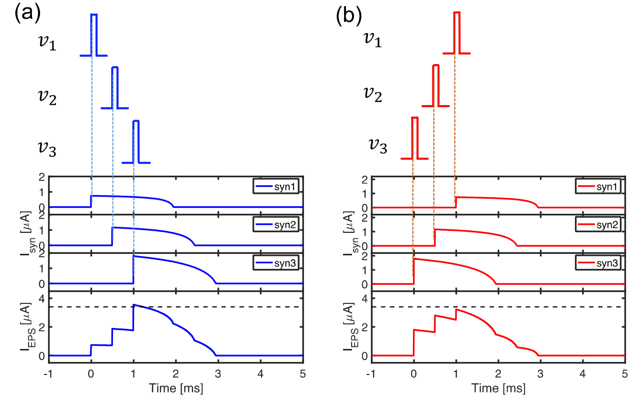

Fig. 12. (a) Synaptic currents (I_{syn}) and total EPSC (I_{EPS}) response for the input spike sequence of [v_1, v_2, v_3] and (b) reversed spike sequence of [v_3, v_2, v_1].

Carlo simulations, the cycle-to-cycle variability of V_T and V_H were computed. Fig. 9 shows the distributions of V_T and V_H, indicating a good agreement between calculations and data.

Fig. 10 shows the statistical distributions of retention time t_R from (a) experimental data and (b) Monte Carlo simulations results at increasing pulse width t_p. In both cases, t_R shows a broad statistical spread, while increasing with t_p on average. The median value of experimental and simulated retention time also shows good agreement [14].

V. Model Application

The dynamic response of the volatile RRAM enables several applications, e.g., exploiting the volatile behavior to mimic the short term plasticity of biological synapse in brain-inspired neuromorphic computing systems [39], [40]. For instance, spatiotemporal learning of spiking patterns was recently demonstrated in RRAM synapses [41], by correlating synaptic weights and spiking times in the same order [42]. However, this concept relies on capacitor-based neurons [42], which might result in large area consumption within the chip [43].

The retention process of volatile RRAM device in the millisecond range provides an alternative approach to spatiotemporal learning. This concept is illustrated in Fig. 11(a), showing the conductance decay of the volatile RRAM after a voltage spike, thus mimicking the short-memory effect. Fig. 11(b) shows the schematic of the circuit with artificial synapses composed of nonvolatile RRAM as synaptic weighting element and volatile RRAM as short-term memory to recognize a spatiotemporal pattern, such as a simple spike sequence. For demonstration, the synapse weights, i.e., the conductance of nonvolatile RRAMs (w_1, w_2, and w_3) is assumed to be in increasing order ($w_1 < w_2 < w_3$). The input spikes are applied to synaptic elements consisting of a nonvolatile RRAM and a volatile RRAM. After the application of the spike, a small read voltage V_{read} is applied and the corresponding total excitatory postsynaptic current (EPSC), denoting as I_{EPS}, was measured.

Fig. 12 shows the synaptic current and total current for the true spike sequence, namely [v_1, v_2, v_3] (a), and the reverse sequence, namely [v_3, v_2, v_1] (b). The discrete spikes activate the time-decaying conductance of the volatile RRAMs, while the current level is controlled by the nonvolatile RRAM weight. As a result, the total current exceeds the true sequence in Fig. 12(a) while the current response to the false sequence remains below the threshold, thus enabling the discrimination of the temporal sequences via the short-term memory in the volatile RRAM. The stochasticity of the relaxation time of the volatile device might result in inaccuracies in recognition of spike sequence. To compensate for stochastic variations, we may adopt multiple volatile devices for each synapse, similar to population coding [44] in the human brain.

VI. Conclusion

A physics-based analytical model of volatile RRAM is presented and validated. The analytical model is based on an extensive mechanism investigation and well captures the electrical characteristics of the device, including dc characteristics, ac responses, and their stochastic variation. We also demonstrate the applications of using this analytical model to simulate the circuit-level behavior where the volatile RRAM is used as short-term memory synapse.

References

[1] M. Wang *et al.*, "Enhancing the matrix addressing of flexible sensory arrays by a highly nonlinear threshold switch," *Adv. Mater.*, vol. 30, no. 33, Aug. 2018, Art. no. 1802516. doi: 10.1002/adma.201802516.

[2] Z. Wang *et al.*, "Memristors with diffusive dynamics as synaptic emulators for neuromorphic computing," *Nature Mater.*, vol. 16, no. 1, pp. 101–108, Jan. 2017. doi: 10.1038/nmat4756.

[3] R. Midya *et al.*, "Anatomy of Ag/Hafnia-based selectors with 10^{10} nonlinearity," *Adv. Mater.*, vol. 29, no. 12, Mar. 2017, Art. no. 1604457. doi: 10.1002/adma.201604457.

[4] Q. Luo *et al.*, "Cu BEOL compatible selector with high selectivity (>10^7), extremely low off-current (~ pA) and high endurance (>10^{10})," in *IEDM Tech. Dig.*, Dec. 2015, pp. 10.4.1–10.4.4. doi: 10.1109/IEDM.2015.7409669.

[5] J. Song, J. Woo, A. Prakash, D. Lee, and H. Hwang, "Threshold selector with high selectivity and steep slope for cross-point memory array," *IEEE Electron Device Lett.*, vol. 36, no. 7, pp. 681–683, Jul. 2015. doi: 10.1109/LED.2015.2430332.

[6] J. Sun *et al.*, "Physically transient threshold switching device based on magnesium oxide for security application," *Small*, vol. 14, no. 27, May 2018, Art. no. 1800945. doi: 10.1002/smll.201800945.

[7] P. Sun *et al.*, "Thermal crosstalk in 3-dimensional RRAM crossbar array," *Sci. Rep.*, vol. 5, Aug. 2015, Art. no. 13504. doi: 10.1038/srep13504.

[8] S. Liu *et al.*, "Eliminating negative-SET behavior by suppressing nanofilament overgrowth in cation-based memory," *Adv. Mater.*, vol. 28, no. 48, pp. 10623–10629, Dec. 2016. doi: 10.1002/adma.201603293.

[9] W. Wang *et al.*, "Surface diffusion-limited lifetime of silver and copper nanofilaments in resistive switching devices," *Nature Commun.*, vol. 10, no. 1, p. 81, Jan. 2019. doi: 10.1038/s41467-018-07979-0.

[10] T. Ohno, T. Hasegawa, T. Tsuruoka, K. Terabe, J. K. Gimzewski, and M. Aono, "Short-term plasticity and long-term potentiation mimicked in single inorganic synapses," *Nature Mater.*, vol. 10, pp. 591–595, Aug. 2011. doi: 10.1038/nmat3054.

[11] M.-K. Kim and J.-S. Lee, "Short-term plasticity and long-term potentiation in artificial biosynapses with diffusive dynamics," *ACS Nano*, vol. 12, no. 2, pp. 1680–1687, Jan. 2018. doi: 10.1021/acsnano.7b08331.

[12] Z. Zhou *et al.*, "Synapse behavior characterization and physical mechanism of a TiN/SiO x/p-Si tunneling memristor device," *J. Mater. Chem. C*, vol. 7, no. 6, pp. 1561–1567, Dec. 2019. doi: 10.1039/C8TC04903C.

[13] W. Wang *et al.*, "Volatile resistive switching memory based on Ag ion drift/diffusion—Part I: Numerical modeling," *IEEE Trans. Electron Devices*, vol. 66, no. 9, pp. 3795–3801, Sep. 2019.

[14] W. Wang, A. Bricalli, M. Laudato, E. Ambrosi, E. Covi, and D. Ielmini, "Physics-based modeling of volatile resistive switching memory (RRAM) for crosspoint selector and neuromorphic computing," in *IEDM Tech. Dig.*, Dec. 2018, pp. 40.3.1–40.3.4. doi: 10.1109/IEDM.2018.8614556.

[15] B. Gao *et al.*, "Modeling disorder effect of the oxygen vacancy distribution in filamentary analog RRAM for neuromorphic computing," in *IEDM Tech. Dig.*, Dec. 2017, pp. 4.4.1–4.4.4. doi: 10.1109/IEDM.2017.8268326.

[16] G. González-Cordero, J. B. Roldán, and F. Jiménez-Molinos, "Simulation of RRAM memory circuits, a Verilog-A compact modeling approach," in *Proc. Conf. Design Circuits Integr. Syst. (DCIS)*, Nov. 2016, pp. 1–6. doi: 10.1109/DCIS.2016.7845386.

[17] A. Padovani, L. Larcher, O. Pirrotta, L. Vandelli, and G. Bersuker, "Microscopic modeling of HfO_x RRAM operations: From forming to switching," *IEEE Trans. Electron Devices*, vol. 62, no. 6, pp. 1998–2006, Jun. 2015. doi: 10.1109/TED.2015.2418114.

[18] N. Lu *et al.*, "A novel method of identifying the carrier transport path in metal oxide resistive random access memory," *J. Phys. D, Appl. Phys.*, vol. 48, no. 6, Feb. 2015, Art. no. 065101. doi: 10.1088/0022-3727/48/6/065101.

[19] W. W. Mullins, "Theory of thermal grooving," *J. Appl. Phys.*, vol. 28, no. 3, pp. 333–339, Mar. 1957. doi: 10.1063/1.1722742.

[20] G. C. Kuczynski, "Self-diffusion in sintering of metallic particles," *Proc. JOM*, vol. 1, no. 2, pp. 169–178, Feb. 1949. doi: 10.1007/BF03398090.

[21] D. Ielmini, "Modeling the universal set/reset characteristics of bipolar RRAM by field- and temperature-driven filament growth," *IEEE Trans. Electron Devices*, vol. 58, no. 12, pp. 4309–4317, Dec. 2011. doi: 10.1109/TED.2011.2167513.

[22] Y. Zhang, S. Zhong, L. Song, X. Ji, and R. Zhao, "Emulating dynamic synaptic plasticity over broad timescales with memristive device," *Appl. Phys. Lett.*, vol. 113, no. 20, Nov. 2018, Art. no. 203102. doi: 10.1063/1.5052556.

[23] W. Steinhögl, G. Schindler, G. Steinlesberger, and M. Engelhardt, "Size-dependent resistivity of metallic wires in the mesoscopic range," *Phys. Rev. B, Condens. Matter*, vol. 66, no. 7, Aug. 2002, Art. no. 075414. doi: 10.1103/PhysRevB.66.075414.

[24] E. H. Sondheimer, "The mean free path of electrons in metals," *Adv. Phys.*, vol. 1, pp. 1–42, Jan. 1952. doi: 10.1080/00018730110102187.

[25] D. Ielmini and Y. Zhang, "Analytical model for subthreshold conduction and threshold switching in chalcogenide-based memory devices," *J. Appl. Phys.*, vol. 102, no. 5, 2007, Art. no. 054517. doi: 10.1063/1.2773688.

[26] S. Ambrogio, S. Balatti, D. C. Gilmer, and D. Ielmini, "Analytical modeling of oxide-based bipolar resistive memories and complementary resistive switches," *IEEE Trans. Electron Devices*, vol. 61, no. 7, pp. 2378–2386, Jul. 2014. doi: 10.1109/TED.2014.2325531.

[27] A. Bricalli, E. Ambrosi, M. Laudato, M. Maestro, R. Rodriguez, and D. Ielmini, "Resistive switching device technology based on silicon oxide for improved ON-OFF ratio—Part II: Select devices," *IEEE Trans. Electron Devices*, vol. 65, no. 1, pp. 122–128, Jan. 2018. doi: 10.1109/TED.2017.2776085.

[28] A. Bricalli, E. Ambrosi, M. Laudato, M. Maestro, R. Rodriguez, and D. Ielmini, "Resistive switching device technology based on silicon oxide for improved ON-OFF ratio—Part I: Memory devices," *IEEE Trans. Electron Devices*, vol. 65, no. 1, pp. 115–121, Jan. 2018. doi: 10.1109/TED.2017.2777986.

[29] Q. Hua *et al.*, "A threshold switching selector based on highly ordered Ag Nanodots for X-point memory applications," *Adv. Sci.*, vol. 6, no. 10, May 2019, Art. no. 1900024. doi: 10.1002/advs.201900024.

[30] Q. Lin *et al.*, "Dual-layer selector with excellent performance for cross-point memory applications," *IEEE Electron Device Lett.*, vol. 39, no. 4, pp. 496–499, Apr. 2018. doi: 10.1109/LED.2018.2808465.

[31] S. Larentis, F. Nardi, S. Balatti, D. C. Gilmer, and D. Ielmini, "Resistive switching by voltage-driven ion migration in bipolar RRAM—Part II: Modeling," *IEEE Trans. Electron Devices*, vol. 59, no. 9, pp. 2468–2475, Sep. 2012. doi: 10.1109/ted.2012.2202320.

[32] F. Ducry *et al.*, "*Ab-initio* modeling of CBRAM cells: From ballistic transport properties to electro-thermal effects," in *IEDM Tech. Dig.*, Dec. 2017, pp. 4.2.1–4.2.4. doi: 10.1109/IEDM.2017.8268324.

[33] S. Yu, B. Gao, Z. Fang, H. Yu, J. Kang, and H.-S. P. Wong, "Stochastic learning in oxide binary synaptic device for neuromorphic computing," *Frontiers Neurosci.*, vol. 7, p. 186, Oct. 2013. doi: 10.3389/fnins.2013.00186.

[34] W. Wang *et al.*, "A hardware neural network for handwritten digits recognition using binary RRAM as synaptic weight element," in *Proc. IEEE Silicon Nanoelectron. Workshop (SNW)*, Jun. 2016, pp. 50–51. doi: 10.1109/SNW.2016.7577980.

[35] H. Jiang *et al.*, "A novel true random number generator based on a stochastic diffusive memristor," *Nature Commun.*, vol. 8, no. 1, p. 882, Oct. 2017. doi: 10.1038/s41467-017-00869-x.

[36] R. Carboni *et al.*, "Random number generation by differential read of stochastic switching in spin-transfer torque memory," *IEEE Electron Device Lett.*, vol. 39, no. 7, pp. 951–954, Jul. 2018. doi: 10.1109/LED.2018.2833543.

[37] R. Degraeve *et al.*, "Quantitative retention model for filamentary oxide-based resistive RAM," *Microelectron. Eng.*, vol. 178, pp. 38–41, Jun. 2017. doi: 10.1016/j.mee.2017.04.032.

[38] S. Ambrogio, S. Balatti, A. Cubeta, A. Calderoni, N. Ramaswamy, and D. Ielmini, "Statistical fluctuations in HfO_x resistive-switching memory: Part I—Set/reset variability," *IEEE Trans. Electron Devices*, vol. 61, no. 8, pp. 2912–2919, Aug. 2014. doi: 10.1109/TED.2014.2330200.

[39] H. Markram, J. Lübke, M. Frotscher, and B. Sakmann, "Regulation of synaptic efficacy by coincidence of postsynaptic APs and EPSPs," *Science*, vol. 275, no. 5297, pp. 213–215, 1997. doi: 10.1126/science.275.5297.213.

[40] S. Kim *et al.*, "Pattern recognition using carbon nanotube synaptic transistors with an adjustable weight update protocol," *ACS Nano*, vol. 11, no. 3, pp. 2814–2822, Mar. 2017. doi: 10.1021/acsnano.6b07894.

[41] W. Wang *et al.*, "Learning of spatiotemporal patterns in a spiking neural network with resistive switching synapses," *Sci. Adv.*, vol. 4, no. 9, Sep. 2018, Art. no. eaat4752. doi: 10.1126/sciadv.aat4752.

[42] W. Wang *et al.*, "Computing of temporal information in spiking neural networks with ReRAM synapses," *Faraday Discuss.*, vol. 213, pp. 453–469, Feb. 2019. doi: 10.1039/C8FD00097B.

[43] T. Tuma, A. Pantazi, M. Le Gallo, A. Sebastian, and E. Eleftheriou, "Stochastic phase-change neurons," *Nature Nanotechnol.*, vol. 11, no. 8, pp. 693–699, 2016. doi: 10.1038/nnano.2016.70.

[44] A. Mizrahi *et al.*, "Neural-like computing with populations of superparamagnetic basis functions," *Nature Commun.*, vol. 9, no. 1, Dec. 2018, Art. no. 1533. doi: 10.1038/s41467-018-03963-w.